JPE 16-3-28

http://dx.doi.org/10.6113/JPE.2016.16.3.1110
ISSN(Print): 1598-2092 / ISSN(Online): 2093-4718

An Inductance Voltage Vector Control Strategy and Stability Study Based on Proportional Resonant Regulators under the Stationary $\alpha\beta$ Frame for PWM Converters

Qiang Sun†, Kexin Wei**, Chenghai Gao*, Shasha Wang***, and Bin Liang**

†,*School of Electrical Engineering and Automation, Tianjin University, Tianjin, China
**Tianjin Key Laboratory of Control Theory & Applications in Complicated Systems, Tianjin University of Technology, Tianjin, China
***Research & Development Department, Tianjin EV Energies Co., Ltd., Tianjin, China

Abstract

The mathematical model of a three phase PWM converter under the stationary $\alpha\beta$ reference frame is deduced and constructed based on a Proportional-Resonant (PR) regulator, which can replace trigonometric function calculation, Park transformation, real-time detection of a Phase Locked Loop and feed-forward decoupling with the proposed accurate calculation of the inductance voltage vector. To avoid the parallel resonance of the LCL topology, the active damping method of the proportional capacitor-current feedback is employed. As to current vector error elimination, an optimized PR controller of the inner current loop is proposed with the zero-pole matching (ZPM) and cancellation method to configure the regulator. The impacts on system's characteristics and stability margin caused by the PR controller and control parameter variations in the inner-current loop are analyzed, and the correlations among active damping feedback coefficient, sampling and transport delay, and system robustness have been established. An equivalent model of the inner current loop is studied via the pole-zero locus along with the pole placement method and frequency response characteristics. Then, the parameter values of the control system are chosen according to their decisive roles and performance indicators. Finally, simulation and experimental results obtained while adopting the proposed method illustrated its feasibility and effectiveness, and the inner current loop achieved zero static error tracking with a good dynamic response and steady-state performance.

Key words: Active damping, Inductance voltage vector, Pole-zero matching, Proportional resonant regulator, Stability

I. INTRODUCTION

Sinusoidal current regulation with low total harmonic distortion (THD) of a 3-phase bidirectional power flowing PWM voltage source converter (VSC) is an aspect of paramount importance to obtain good performance in many different applications, such as active power filters, motor drives, variable-speed wind turbines and photovoltaic inverters [1]-[8]. As a result, the research and development of various methods in the field of current regulators have been put forward to realize good power quality for VSCs. Over the past few years, pulse width modulation (PWM) and hysteresis controls with their optimization have been popularly adopted due to their advanced features [5]-[9]. Hysteresis modulation introduces a minor error to the average current and offers much better dynamic current tracking than the PWM method. However, the inherent disadvantage is its variable switching frequency, which makes it rather difficult to design a power filter for harmonics attenuation and to reduce the switching loss for efficiency improvement [5]. Some researchers have proposed a nonlinear sliding mode variable structure approach based on the adaptive band

Manuscript received May 21, 2015; accepted Jan. 26, 2016
Recommended for publication by Associate Editor Sangshin Kwak.
†Corresponding Author: sunqiang@tju.edu.cn
Tel: +86-13920170309, Tianjin University
*School of Electrical Eng. and Automation, Tianjin University, China
**School of Electrical Eng., Tianjin University of Technology, China
***R&D Department, Tianjin EV Energies Co., Ltd., China

hysteresis theory, and a lot of effort has been done to achieve a fixed switching frequency. However, obtaining a high-frequency chatter free switching frequency on the sliding surface requires prior knowledge of the upper bounds of the system uncertainties [6]. Space vector modulation (SVM) is a widely used PWM strategy due to its constant switching frequency, and because its chosen switching sequence can be easily implemented with Park transformation [7], [8]. Meanwhile, this voltage oriented control divides alternating current into two parts, active and reactive segments, and then controls them separately with linear PI regulators, which achieves a good dynamic response by the inner current control loop with accurate decoupling calculations and proportional-integral regulating [9]. Some alternative control algorithms have been proposed such as instance predictive control [10], direct power control (DPC) [11], [12], deadbeat control [13]-[15], etc. The main principle of the DPC method is to directly regulate the instantaneous power instead of using the inner current loop, which will produce serious power ripples and a variable switching frequency along with pre-defined on-off forms and hysteresis comparators. In addition, the main shortcoming of the deadbeat strategy is its request for a small sampling period so as to achieve satisfactory performance. In terms of the inner current-loop controllers, there are some approaches to improve system characteristics of the PWM converter. A great deal of effort has been expended to tackle the above problems for tracking error cancellation. PI and PR approaches have been widely adopted in linear tuning strategies. The control of the VSC can be implemented under different reference frames, such as the *abc*, *αβ* or *dq* reference frames. Detailed information on the reference frames for the VSC is introduced in [4]. There is strong coupling between the *d* and *q*-axes for a PI regulator, and sinusoidal values lead difficulty in precisely tracking the reference AC signals without a static error [16], [17]. For solving this issue, a PR controller is introduced into the inner current loop [18]-[22]. Thus, the steady state error of a specific frequency can be completely removed since this ideal PR controller provides an infinite gain and a 180° phase shift at the points where the stability problem is produced. Nevertheless, unlike the PI controller, the PR controller is generally complicated to design for whole control systems with stability [22].

In addition, the harmonics generated by converters having an impact on other grid connected utilities and devices are limited by IEEE 519-2014, which presents limits for the THD of currents. Therefore, it is important to do filter studies for eliminating current harmonics [23]-[25]. A third order LCL-filter is quite suitable for grid-tied VSCs with good performance in current ripple attenuation even with small inductances. In addition, an LCL filter exhibits an undesired resonance effect that causes stability problems. A passive damping method has good reliability and simplicity, but it leads to a lot of power dissipation [26]. These problems can be addressed by adopting the capacitor current feedback strategy of active damping, since it has better robustness to external disturbances than passive damping when the line current includes lots of harmonics [27], [28]. However, the damping regulator introduces a voltage component into the VSC modulation index reference that is difficult to achieve for the traditional DPC. This is due to the fact that the PWM modulation is not directly controlled via the inner current loop. Thus, it can be tackled through a collaboration between the deadbeat predictive power control approach and an optimized PR regulator under the stationary *αβ* reference frame with the SVM. This is done to obtain a high dynamic instantaneous active and reactive power track with a variable on-off frequency prevention and a relatively satisfactory performance. Normally, the system's stability margin and characteristics can be illustrated by the means of the steady-state error, crossover frequency, phase margin (PM), and gain margin (GM) [17]. As a result, the above mentioned methods can be employed for the system parameter and robustness design of the current controller and the capacitor-current-feedback active-damping.

First, this paper analyzes the mathematical model of a three-phase grid connected VSC under the stationary *αβ* reference frame, and then presents an accurate calculation of the inductance voltage vector approach with a predictive power control outer loop. The impact of parameter variations on an inner-current loop adopting an active damping PR regulator on the system dynamic and static performance is mechanismly studied. Furthermore, the stability problem and optimal parameter configuration of the control block diagram correctly addressed by considering the pole-zero assignment method of the frequency domain response are also reviewed and discussed. A specific and effective approach for the control of an active damping LCL-topology-based VSC with a PR controller is proposed. Finally, simulation and experimental results are presented in a systematic way to verify the theoretical concepts and implementation is discussed throughout the whole presentation.

II. Calculation Method of the Reference Voltage

A grid-connected 3-phase VSC adopting an LCL-filter is illustrated in Fig. 1, where L_g, L_r and C_f are the grid-side inductor, converter-side inductor and branch capacitor respectively, and the VSC typically consists of a 3-phase IGBT bridge and a DC side electrolytic capacitor.

The following equation could be defined by *Kirchhoff Law* when system is under the rectifier mode.

$$\begin{cases} V_{Lk} = U - V_k - \left(R_{L_g} I_g + R_{L_r} I_r \right) \\ I_g = I_c + I_r \end{cases} \tag{1}$$

Where V_{dc} and i_{dc} are the DC-link voltage and current, R_L is

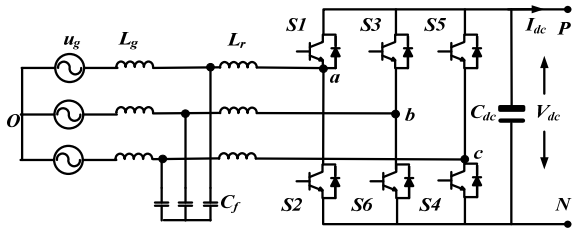

Fig. 1. Topology diagram of three-phase PWM converter.

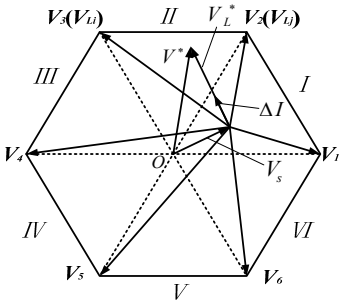

Fig. 2. Distribution of inductance voltage vectors for different switching states.

the equivalent resistance considering the line impedance and series resistance of the inductors L_g and L_r, V_L is inductance voltage vector, and V_k is the converter average voltage vector. Thus, the corresponding inductance voltage vector can be represented as:

$$V_{Lk} = \left[U - \left(R_{L_g} + R_{L_r}\right) I_g + R_{L_r} I_c\right] - V_k \tag{2}$$

To achieve the real parameter values of the series resistance, capacitor and reactor, a Precision Impedance Analyzer WK6500B is employed. Thus, the following expression can be written, considering (1) and (2), as:

$$\begin{cases} V_s = U - \left(R_{L_g} + R_{L_r}\right) I_g + R_{L_r} I_c \\ V_k = V_s - V_{Lk} \end{cases} \tag{3}$$

To realize the actual current tracking its reference, the vector direction of *di/dt* should be approximately the same as *–ΔI*. This is equivalent to seeking the corresponding V_k with the smallest included angle between *-ΔI* and *-*V_{Lk}, as shown in Fig. 2.

The equivalent control model for the VSC is generally achieved by neglecting the influence of the series resistance *R* [8], [25], [27]. However, through the observation of (3) and Fig. 2 of the inductance voltage vectors distribution, the series resistance directly impacts the calculation accuracy for the reference inductance voltage vector selection, and the resistance value for underestimating or overestimating has large effects on the integral absolute error although it is relatively small, as described Dr. Ana Vidal and Dr. Alejandro G. Yepes at the University of Vigo [29]. The function *IAE* should be defined to identify the underestimated and overestimated cases. The error *ε(k, t)* between both the curves and the integral absolute error *IAE(k)* are calculated. *IAE* is decided through the area covered between the two curves $i^{R=R'}$ and $i^{R\neq R'}$. Moreover, the sign of the error area is

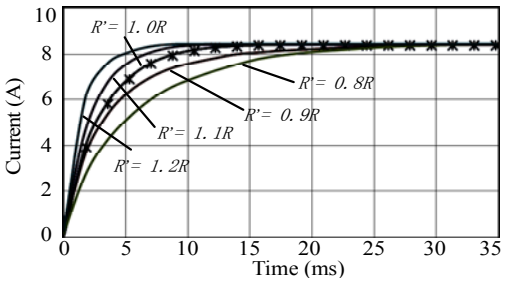

Fig. 3. Effects of *WIAE* for *R' = R*, *R' > R* and *R' < R*.

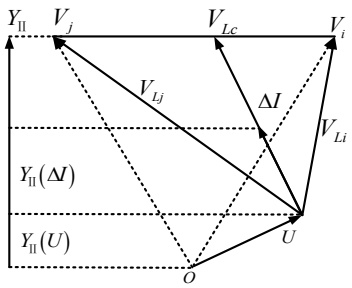

Fig. 4. Distribution of voltage vector V_{Lc} and reference axis Y_{II}.

calculated via the integral error *IE(k)*.

$$\begin{cases} \varepsilon(k,t) = i^{R=R'}(k,t) - i(k,t) \\ IE(k) = \Sigma_{t=0}^{t_{sto}} \varepsilon(k,t) \cdot T_s \\ IAE(k) = \Sigma_{t=0}^{t_{sto}} \left|\varepsilon(k,t)\right| \cdot T_s \end{cases} \tag{4}$$

By this means, the weighted *IAE* (*WIAE*) can be defined as:

$$WIAE(k) = \begin{cases} IAE(k), & if \quad IE(k) \geq 0 \\ \left[IAE(k)\right]^2, & if \quad IE(k) < 0 \end{cases} \tag{5}$$

As in the above analysis, the cost function *IAE* illustrates considerable influence on accurate reference vector selection, and the area between $i^{R=R'}$ and $i^{R\neq R'}$ is relatively less when overestimating than when underestimating. Thus, a LCR analyzer WK6500B for precise vector computation in the VSC control strategy, which characterizes components up to 120 MHz with 0.05% basic measurement accuracy, can generally satisfy the requirement. And equation (4) and (5) along with Fig. 3 theoretically verified whole analysis.

Define the inductance voltage vector V_{Lc}, which is composed by the adjacent vectors V_{Li} and V_{Lj}, is in the same direction, as *ΔI* in Fig. 4. Assume the parameter *Γ* as follows.

$$\Gamma = \frac{\Delta I}{V_{Lc}} \tag{6}$$

Define T_{des} as the vector composition period of V_{Li} and V_{Lj} for *ΔI* elimination.

$$T_{des} = L\Gamma \tag{7}$$

The reference inductance voltage vector can be expressed as follows.

$$\begin{cases} T_s = L\Gamma \,\&\, V_L^* = L\Delta I / T & (L\Gamma \leq T) \\ T_s = T \,\&\, V_L^* = \Delta I / \Gamma & (L\Gamma > T) \end{cases} \tag{8}$$

In order to calculate the parameter *Γ*, the reference axes Y_S are needed. They are located in six sectors and are

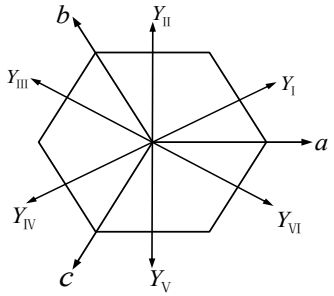

Fig. 5. Distribution of reference axis Y_S.

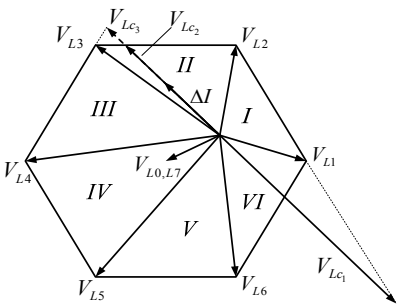

Fig. 6. Location of ΔI and distribution of V_{Lc1}, V_{Lc2} and V_{Lc3}.

perpendicular to axes a, b and c, as shown in Fig. 5. Assume that $Y_{II}(\Delta I)$, $Y_{II}(V_{Lc})$ and $Y_{II}(U)$ are projections of ΔI, V_{Lc} and U on the reference axis Y_{II}. Since ΔI and V_{Lc} are in the same direction, the parameter Γ can be calculated via (7) and (8).

$$\Gamma=\frac{|Y_{\mathrm{II}}(\Delta I)|}{|Y_{\mathrm{II}}(V_{Lc})|}=\frac{|Y_{\mathrm{II}}(\Delta I)|}{|Y_{\mathrm{II}}(V_i)|-|Y_{\mathrm{II}}(U)|}=\frac{|Y_{\mathrm{II}}(\Delta I)|}{\left(\sqrt{3}\right)^{-1}v_{dc}-|Y_{\mathrm{II}}(U)|} \tag{9}$$

Therefore, if the reference frame of a certain sector is confirmed, the parameter Γ of this sector will be obtained.

Each sector corresponds to a pair of adjacent inductance voltage vectors V_{Li} and V_{Lj} as shown in Fig. 6. Assume that ΔI is located in the region S, the reference axis Y_S should be used to calculate Γ.

$$\Gamma=\frac{|Y_S(\Delta I)|}{\left(\sqrt{3}\right)^{-1}v_{dc}-|Y_S(U)|} \tag{10}$$

The following vector and variables are defined.

$$\begin{cases}\Delta I=\Delta i_a+\Delta i_b e^{j2\pi/3}+\Delta i_c e^{-j2\pi/3}\\ U=u_a+u_b e^{j2\pi/3}+u_c e^{-j2\pi/3}\\ V^*=v_a^*+v_b^* e^{j2\pi/3}+v_c^* e^{-j2\pi/3}\end{cases} \tag{11}$$

When ΔI is located in section II, the projection value can be obtained as $|Y_{\mathrm{II}}(\Delta I)|=\left(\sqrt{3}\right)^{-1}(\Delta i_b-\Delta i_c)$ and $|Y_{\mathrm{II}}(U)|=\left(\sqrt{3}\right)^{-1}(u_b-u_c)$, which is substituted into (10) for the calculation of Γ. Thus, Γ with all of the conditions is obtained as shown in Table I by parity of reasoning.

In addition, as to the outer control loop, according to the instantaneous power theory and the equivalent coordinate transformation, the system's instantaneous power S can be derived by multiplication between the voltage vector and the current vector conjugate, and it is expressed as follows:

TABLE I
COMPUTATION OF EACH SECTOR'S Γ

Sector	I	II	III
Γ	$\frac{\Delta i_a-\Delta i_c}{v_{dc}+u_c-u_a}$	$\frac{\Delta i_b-\Delta i_c}{v_{dc}+u_c-u_b}$	$\frac{\Delta i_b-\Delta i_a}{v_{dc}+u_a-u_b}$
Sector	IV	V	VI
Γ	$\frac{\Delta i_c-\Delta i_a}{v_{dc}+u_a-u_c}$	$\frac{\Delta i_c-\Delta i_b}{v_{dc}+u_b-u_c}$	$\frac{\Delta i_a-\Delta i_b}{v_{dc}+u_b-u_a}$

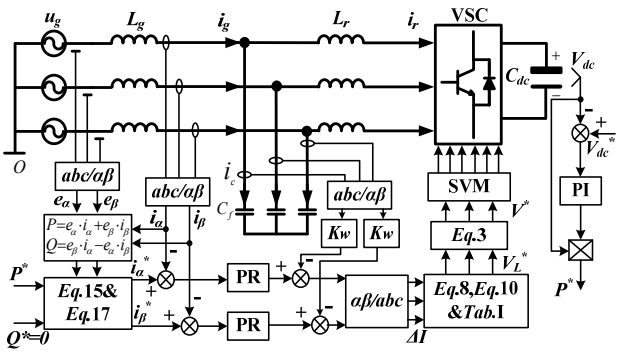

Fig. 7. Deadbeat predictive instantaneous power control strategy with PR controller based on inductance voltage vector under $\alpha\beta$ frame.

$$S=\frac{3}{2}u\cdot i^*=\frac{3}{2}\left(u_\alpha i_\alpha+u_\beta i_\beta\right)-j\frac{3}{2}\left(u_\alpha i_\beta-u_\beta i_\alpha\right) \tag{12}$$

Define $v_{\alpha\beta}=[v_\alpha\ v_\beta]^T$, $u_{\alpha\beta}=[u_\alpha\ u_\beta]^T$ and $i_{\alpha\beta}=[i_\alpha\ i_\beta]^T$ as the average voltage vector of the VSC, and the line voltage and current vectors in the stationary $\alpha\beta$ frame, respectively.

Under the α–β plane, the instantaneous active and reactive power model of the three-phase VSC is defined as follows.

$$\begin{bmatrix}P\\Q\end{bmatrix}=\frac{3}{2}\begin{bmatrix}u_\alpha & u_\beta\\ u_\beta & -u_\alpha\end{bmatrix}\begin{bmatrix}i_\alpha\\ i_\beta\end{bmatrix} \tag{13}$$

Assume that the line voltage $u_{\alpha\beta}$ during instant T_s is ideally invariant ($u_{\alpha\beta}(k+1)=u_{\alpha\beta}(k)$). Consequently, the algebraic iterative expression of the instantaneous powers during 2 continuous sampling periods is observed as:

$$\begin{bmatrix}P(k+1)-P(k)\\ Q(k+1)-Q(k)\end{bmatrix}=\frac{3}{2}\begin{bmatrix}u_\alpha(k) & u_\beta(k)\\ u_\beta(k) & -u_\alpha(k)\end{bmatrix}\cdot\begin{bmatrix}i_\alpha(k+1)-i_\alpha(k)\\ i_\beta(k+1)-i_\beta(k)\end{bmatrix} \tag{14}$$

To achieve the aim of the predictive control, the controlled object is adjusted to track its dynamical given values by the next period as shown in the following expression.

$$\begin{cases}i_{\alpha\beta}(k+1)=i_{\alpha\beta}^*(k)\\ P(k+1)=P^*(k)\\ Q(k+1)=Q^*(k)\end{cases} \tag{15}$$

Accordingly, the converter average voltage vector is expressed as follows:

$$\begin{bmatrix}v_\alpha\\ v_\beta\end{bmatrix}=\begin{bmatrix}u_\alpha\\ u_\beta\end{bmatrix}-\frac{2}{3}\frac{L}{T_s\|u_{\alpha\beta}\|^2}\begin{bmatrix}u_\alpha & u_\beta\\ u_\beta & -u_\alpha\end{bmatrix}\begin{bmatrix}P(k+1)-P(k)\\ Q(k+1)-Q(k)\end{bmatrix} \tag{16}$$

The reference input current in the α-β plane by the transformations from (14)-(16) can be performed by means of the following relation:

$$\begin{bmatrix} i_\alpha^* \\ i_\beta^* \end{bmatrix} = \frac{2}{3}\frac{1}{\left\|u_{\alpha\beta}\right\|^2}\begin{bmatrix} u_\alpha & u_\beta \\ u_\beta & -u_\alpha \end{bmatrix}\begin{bmatrix} \varepsilon_P \\ \varepsilon_Q \end{bmatrix} + \begin{bmatrix} i_\alpha \\ i_\beta \end{bmatrix} \tag{17}$$

Therefore, the topology of the proposed current control strategy adopting a PR regulator under the stationary $\alpha\beta$ frame for a PWM converter is shown in Fig. 7.

III. Robustness Design of the Current Regulator

The transfer function under the α-β plane of a PI regulator achieved by a positive or negative-sequence is computed via the usage of the frequency shift adopting internal model control, and the optimized state transformation or frequency domain approach of a PR regulator is presented, which directly regulates the overall current, including both the positive and negative components under stationary $\alpha\beta$ coordinates [21], [30]. An ideal PR regulator has an infinite gain and a 180° phase shift at the fundamental frequency ω_0, and it has little phase shift and gain except for ω_0. In order to solve the stability problems caused by an infinite gain, an optimized PR regulator can be used in practical implementations with a finite gain, but high enough to achieve little static error [18], [19]. The improved PR controller is in the following form:

$$G_{PR}(s) = K_P + \frac{2K_R\omega_c s}{s^2 + 2\omega_c s + \omega_0^2} \tag{18}$$

Where K_P and K_R are the proportional and resonant coefficients, ω_c is represents the bandwidth at -3 dB which can enhance the robustness and stability in the presence of line frequency variations.

A. Model and Control of the System

For the inner current control loop, the grid side inductor current i_g is compared with its reference i_g^* and produces an error into the PR regulator. This generates a given current value i_c^*. The capacitor current i_c is fed back to adapt i_c^*, and along with the proportion loop for active damping to produce the modulation reference for the converter. Therefore, the control block diagram can be derived as follows.

In terms of Mason's Rule and the system model, the input current expression can be introduced as:

$$i_g = \frac{G_{PR}(s)\cdot G_D(s)\cdot G_{VSC}(s)\cdot G_{LCL}(s)}{1+G_{PR}(s)\cdot G_D(s)\cdot G_{VSC}(s)\cdot G_{LCL}(s)} i_g^* - \frac{G_{LCL}(s)}{1+G_{PR}(s)\cdot G_D(s)\cdot G_{VSC}(s)\cdot G_{LCL}(s)} e \tag{19}$$

By (19), the gain of $G_{PR}(s)\cdot G_D(s)\cdot G_{VSC}(s)\cdot G_{LCL}(s)$ at the control system's resonant frequency is much larger than 1. Thus, the first item approximation of (19) is 1, and the grid voltage disturbance is approximately 0. The transfer function of the system current open loop is derived as:

$$G(s) = \frac{i_g}{i_g^* - i_g} = G_{PR}(s)\cdot G_D(s)\cdot G_{VSC}(s)\cdot G_{LCL}(s) \tag{20}$$

Instability will be led to by a time delay of the calculation and the PWM loop [31], [32]. In addition, the first-order delay is on behalf of the *ZOH* of the VSC current. In addition, the delay T_d is considered to represent a digital implementation of the computational delay. The Taylor series expansion is used for modeling approximations of the two first-order inertial elements.

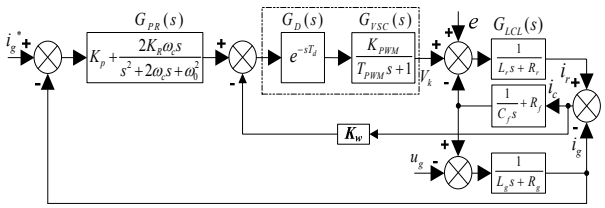

Fig. 8. Control block diagram of inner current loop.

$$\begin{aligned} G_P(s) &= e^{-T_d s}\cdot\frac{K_{PWM}}{T_{PWM}s+1} \\ &\approx \frac{K_d}{T_d s+1}\cdot\frac{K_{PWM}}{T_{PWM}s+1} \approx \frac{K_D}{\sum T_i s+1} \end{aligned} \tag{21}$$

For a three phase PWM converter with synchronous sampling of the input current and with a sampling period T_s, the total time delay including the sampling and transport delay is generally given by $\sum T_i = 1.5T_s$.

The active damping technique using capacitor current feedback in Fig. 7 is a type of control algorithm rather than physical elements. After the introduction of a second order oscillation element by the active damping gain K_w to suppress resonance peak, its Laplace transfer function becomes:

$$G_{LCL}(s) = \frac{1}{L_g L_r C_f s\left(s^2 + \frac{K_w}{L_r}s + \frac{L_g+L_r}{L_g L_r C_f}\right)} \tag{22}$$

The system order is added greatly after employing a PR regulator. Thus, the equivalent expression of (20) can be written in the form of (23).

$$G(s) = \frac{a_2 s^2 + a_1 s + a_0}{b_6 s^6 + b_5 s^5 + b_4 s^4 + b_3 s^3 + b_2 s^2 + b_1 s + b_0} \tag{23}$$

Where, $a_0 = K_p\omega_0^2$, $a_1 = 2\left(K_p + K_R\right)\omega_c$, $a_2 = K_p$, $b_0 = 0$, $b_1 = \left(L_g + L_r\right)\omega_0^2$, $b_2 = \left(L_g + L_r\right)\left(2\omega_c + \sum T_i\omega_0^2\right) + L_g C_f K_w\omega_0^2$, $b_3 = \left(L_g + L_r\right)\left(2\omega_c\sum T_i + 1\right) + \left(2\omega_c + \sum T_i\omega_0^2\right)L_g C_f K_w + \omega_0^2 L_g L_r C_f$, $b_4 = \left(L_g + L_r\right)\sum T_i + \left(2\omega_c\sum T_i + 1\right)L_g C_f K_w + \left(2\omega_c + \sum T_i\omega_0^2\right)L_g L_r C_f$, $b_5 = \sum T_i L_g C_f K_w + \left(2\omega_c\sum T_i + 1\right)L_g L_r C_f$, $b_6 = \sum T_i L_g L_r C_f$.

The damping ratio can be written as:

$$\zeta = \frac{K_w}{2}\sqrt{\frac{L_g C_f}{\left(L_g + L_r\right)L_r}} \tag{24}$$

With the damping ratio ζ increasing gradually from 0 to 0.9, the resonance peak of the transfer function $G_{LCL}(s)$ changes from 30dB to disappearance, so as to effectively restrain the amplification effect at the resonance frequency point, which is illustrated in Fig. 9. Since a larger K_w leads to the controller's saturation and stability, the parameters are chosen as ζ=0.707 and K_w=1.36 based on the good convergence performance of the second-order optimal theory.

The controller's bandwidth ω_c reflects the ability to track

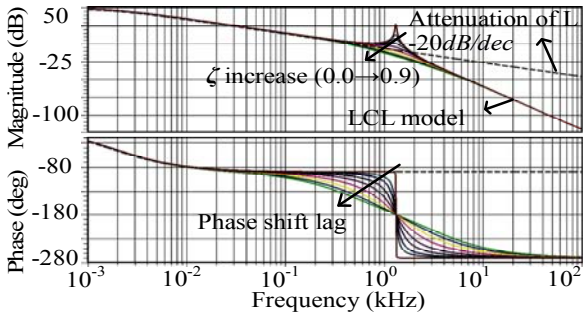

Fig. 9. Bode frequency characteristics corresponding to variable damping coefficient.

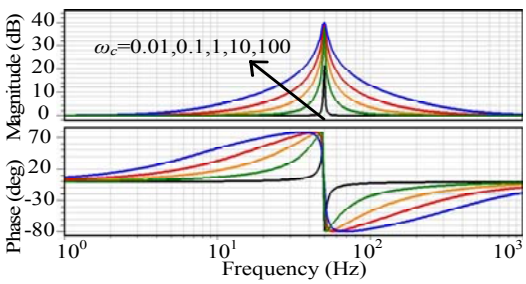

Fig. 10. Frequency response of resonant term for variation in ω_c.

the input signal. Therefore, the system should have a larger bandwidth in order to enhance the dynamic response characteristics [20], [21]. However, high frequency interference noise such as the switching frequency affects the system's stability when ω_c increases. The change rule for this is depicted in Fig. 10. Since the VSC is required to run well while the grid fundamental frequency fluctuates between 49.5 Hz and 50.5 Hz [17], $\omega_c = 2\pi\Delta f = \pi$ rad/s is defined to get a lot of gain in whole operating frequency scale with a related maximum frequency variation of $\Delta f = 0.5$ Hz.

B. Influence of System Parameters on the Root Locus

The six-order system in (23) is a little too complex to get a practical solution. It shows that there are two zeros and the Bode diagram in Fig. 9 shows that the general derivation LCL topology behaves like L at frequencies lower than the approximate resonant frequency [29]. Compared with the original system, it is easier to calculate with pole-zero cancellation from six to four. As illustrated in Fig. 11, the control target is to configure P_1 and P_2 as the dominant poles of a second order under-damped linear element with ζ=0.707, and the distance of P_3 and P_4 off the imaginary axis is 5 times bigger than that of the dominant poles. This ensures stability with enough of a margin for system parameter variations. As shown in the following analysis, parameter-corresponding pole-zero locus for the closed-loop transfer function is employed for optimal parameter configuration.

From Fig. 11(a), when the equivalent inductance L is increasing, the system's poles distribution moves off the imaginary axis although its impact on the pole-zero locus of the system is relatively less. This improves the system stability. Thus, a good robustness to reactor value variations

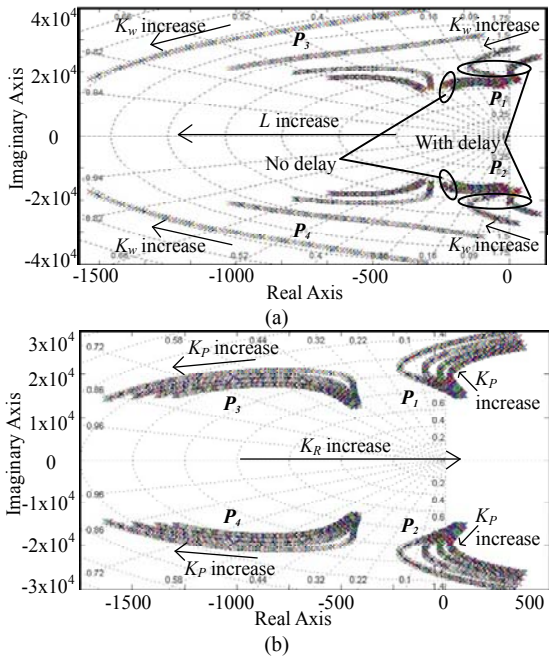

Fig. 11. Pole-zero locus of inner current loop corresponding to variable parameter value. Arrows show the variation of pole placement. (a) With variable K_w, $\sum T_i$ and L. (b) With variable K_P and K_R.

can be achieved. When the active damping coefficient K_w increases, the root locus of the dominant poles P_1 and P_2 moves from instability in the right half plane to a stable state with damp increasing, and then into the instable region again after the critical value is reached with K_w=1.4. This is in accordance with the optimum value mentioned above. Correspondingly, the poles P_3 and P_4 lean to shift far off of the imaginary axis with the system damp increasing and good resonance peak suppression. Meanwhile, the poles generated from the LCL-filter and PR controller shift quickly near the imaginary axis while the total delay $\sum T_i$ increases. It can be seen that the parameters scale that leads to system instability is extended with a time delay. This makes the controller and poles hard to configure. From Fig. 11(b), K_P and K_R should be determined via the predicted placement of P_1 and P_2 so that the damping ratio and inherent frequency are involved. When K_P increases, the dominant poles shift off of the imaginary axis and then near it, when the system's damp changes from 'large' to 'small.' This has almost as much influence as K_w. K_R has less influence on the root locus than K_P. This leads to the poles shifting near the imaginary axis. Thus, its damping is decreased. It is well-known that K_P is directly related to the dynamic performance of regulator. However, K_R mainly decides its gain at a specific frequency and adjusts its bandwidth close to the resonance. According to the pole-zero locus, a parameters scale that meets the system stability and performance requirements can be obtained.

Based on the principle discussed above, the rules of the parameters' influence are illustrated, and their optimal ranges are derived. The frequency response of the system Bode and

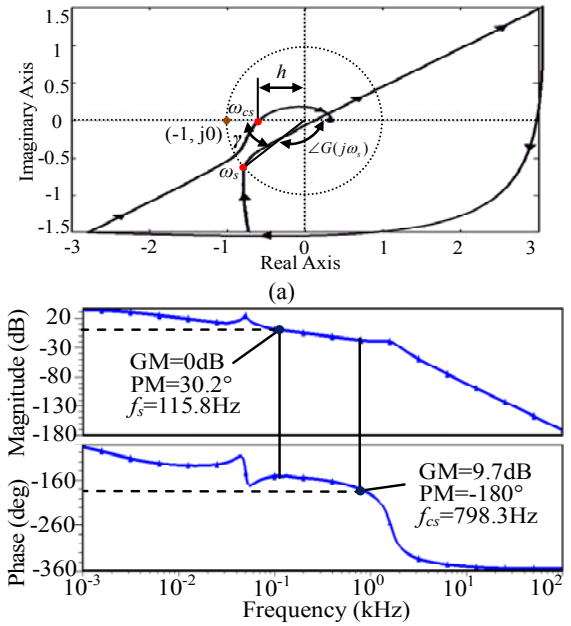

Fig. 12. Frequency response performance of current loop. (a) Overview of Nyquist diagram. (b) Bode plot diagram.

Nyquist diagram with selected optimal parameters is depicted in Fig. 12. In terms of the Nyquist theory, the control system is for stability since its trajectory does not encircle the critical point (*-1, j0*) [33]. Compared with the original continuous s-domain model, they have an amplitude margin of $h=-20\lg\left|G\left(j\omega_{gs}\right)\right|=9.7dB$ and a phase margin of $\gamma=\pi+\angle G\left(j\omega_{cs}\right)=30.2°$ at the cross over frequency. In addition, the corresponding frequency of the dominant poles at -3dB is about 220Hz, which is far enough from the fundamental frequency. This is good for the system's characteristics. Consequently, the phase and amplitude margin guarantees the control system's stability.

C. Digital Implementation of the Current Regulator

Generally, the current regulator is analyzed under the continuous time domain and it is necessary to adopt an appropriate discretization approach in the digital control system, such as the Tustin (bilinear transformation), first-order hold, and impulse invariance to guarantee the discrete domain of current controller can accurately match its continuous model [14], [31], [33]. In addition, an inappropriate discretization method leads to the zeros and poles shifting in terms of the system's transfer function, which may deteriorate controller's stability and decrease its tracking precision.

During the discretization procedure, the impacts of aliasing distortion in the impulse invariance method are indistinguishable from the original continuous model. In addition, the time lagging response and frequency shift in the Tustin method lead to an unsatisfied frequency response as a result of the continuous s-domain transfer function [33]. In order to improve the signal tracking precision in a practical system, the ideal digital implementation approach cannot cause a gain attenuation or phase shift at the resonant frequency. To solve the above problems during the controller's discretization, the zero-pole matching (ZPM) discipline is predicted as follows:

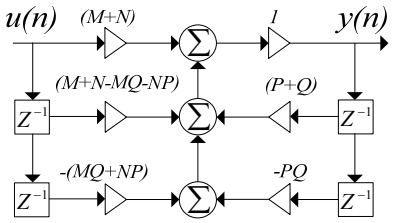

Fig. 13. Digital implementation diagram of controller.

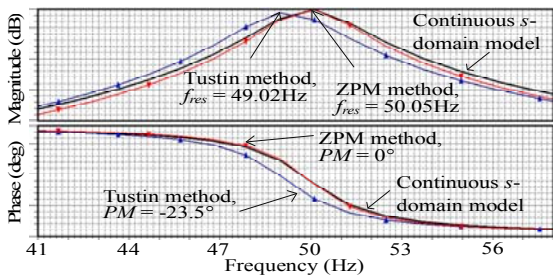

Fig. 14. Discretization results adopting Tustin and ZPM method with 4 kHz sample frequency.

$$\begin{cases} D(s)=\dfrac{k\prod_i(s+z_i)}{\prod_j(s+p_j)} \\ D(z)=\dfrac{k_0\prod_i(z-e^{-z_iT_s})}{\prod_j(z-e^{-p_jT_s})}(z+1)^{j-i} \end{cases} \tag{25}$$

There are proportional and resonant parts for a PR controller. The proportional part is linear with a small constant coefficient K_p. Thus, the controller's discretization derivation about the resonant segment is as follows.

$$\begin{aligned} G_R(s)&=\frac{2K_R\omega_c s}{s^2+2\omega_c s+\omega_0^2} \\ &=\frac{M}{s+\omega_c-\sqrt{\omega_c^2-\omega_0^2}}+\frac{N}{s+\omega_c+\sqrt{\omega_c^2-\omega_0^2}} \end{aligned} \tag{26}$$

Where, $M=K_R\omega_c(1-\frac{\omega_c}{\sqrt{\omega_c^2-\omega_0^2}})$ and $N=K_R\omega_c(1+\frac{\omega_c}{\sqrt{\omega_c^2-\omega_0^2}})$.

Define $p_1=\omega_c-\sqrt{\omega_c^2-\omega_0^2}$ and $p_2=\omega_c+\sqrt{\omega_c^2-\omega_0^2}$, and according to the zero-pole matching rule shown in (25), the discretization result of the PR controller using the ZPM method is derived as follows:

$$G_R(z)=\left(\frac{M}{z-e^{-p_1T_s}}+\frac{N}{z-e^{-p_2T_s}}\right)(z+1) \tag{27}$$

Define $P=e^{-p_1T_s}$ and $Q=e^{-p_2T_s}$, and then the transfer function in the z domain can be obtained.

$$G_R(z)=\frac{(M+N)+(M+N-MQ-NP)z^{-1}-(MQ+NP)z^{-2}}{1-(P+Q)z^{-1}+PQz^{-2}} \tag{28}$$

From (28), the differential expression to be coded for the discrete-time implementation can be written as:

$$y(n) = (P+Q)\cdot y(n-1) - PQ\cdot y(n-2) + (M+N)\cdot u(n) + (M+N-MQ-NP)\cdot u(n-1) - (MQ+NP)\cdot u(n-2) \quad (29)$$

Equation (29) is implemented by using the digital implementation structure shown in Fig. 13.

As shown in Fig. 14, the discretization results using the zero-pole matching method can offer reasonable positions for the system's resonant peaks and a similar frequency response as the continuous transfer function. When the Tustin method is applied, due to its simple calculation, the results are quite unsatisfactory. The resonant frequency shifts from 50 Hz to 49.02 Hz, and phase response has a delay of −23.5°, which is harmful to the regulator stability. Define ω_A as the angular frequency of the continuous time domain and ω_D as the the angular frequency of discrete-time domain, so the transformation mechanism from continuous to the discrete domain via Tustin is written as following substitution.

$$s = \frac{2}{T_s}\frac{1-z^{-1}}{1+z^{-1}} \Leftrightarrow j\omega_A = \frac{2}{T_s}\frac{1-e^{-j\omega_D T_s}}{1+e^{-j\omega_D T_s}} = \frac{2}{T_s}\frac{2j\sin\left(j\omega_D T_s/2\right)}{2\cos\left(j\omega_D T_s/2\right)} = j\frac{2}{T_s}\tan\frac{\omega_D T_s}{2} \quad (30)$$

The expression $\omega_A = {}^{2}\!/_{T_s}\tan\left({}^{\omega_D T_s}\!/_{2}\right)$ is obtained, and when the sampling frequency is quite fast, the approximate equation $\omega_A \approx \omega_D$ can be reached theoretically. Thus, the ZPM method has better performance due to the accurate zero/pole transformation and mapping between the two domains without frequency aliasing distortion and phase shift.

IV. Simulation and Experimental Results

A. Simulation Results

In this section, the results of the described mathematical analysis and the effectiveness of the suggested strategy have been verified by means of numerical simulations. The system's parameters are listed in Table II.

Fig. 15 and Fig. 16 show the AC-side current trajectory presented in this paper compared with the traditional SVM. The three marked sections of the trajectory mean: [I] the rectifier state, [II] the inverter state, and [III] the state that limits the amplitude of the current. The dynamic tracking performance of the proposed solution is much better than that of the traditional SVM.

It can be observed from Figs. 17-20, that the instantaneous power and the DC voltage both track each reference and include good stability and little static error. The input current has an almost sinusoidal waveform (THD = 2.38%) and is synchronous to the grid voltage. Thus, the unity power factor running of the VSC is successfully implemented with a reactive power that is approximately zero.

B. Experimental Verification

TABLE II
Parameters of Active-Damping LCL VSC Prototype

Parameter	Value
Grid voltage U_g (RMS)	50 V
Grid current I_g (RMS)	30 A
Grid side inductance L_g	0.25 mH
Converter side inductance L_r	0.50 mH
Branch capacitor C_f	116 uF
DC-BUS capacitor C_{dc}	4700 uF
Grid frequency f_1	50 Hz
Switching frequency f_{sw}	2.0 kHz
Sampling period T_s	0.25 ms

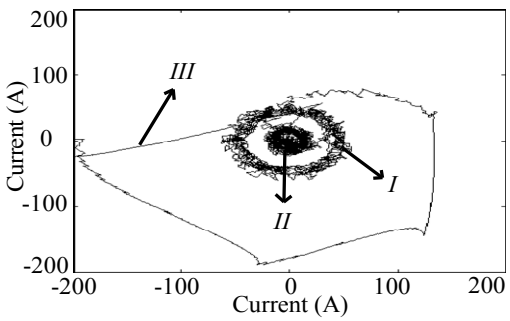

Fig. 15. The trajectory of the current vector I under traditional DPC-SVM.

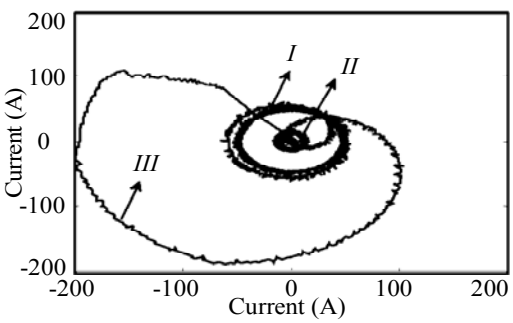

Fig. 16. The trajectory of the current vector I under proposed method.

The considered grid-connected VSC prototype with a LCL-filter has been experimentally tested according to the design strategy proposed in this paper. The parameters of the system are reported in Table II and a PR regulator is designed as analyzed in Section III.

The voltage and current waveforms of phase A both at the VSC and the grid sides are shown in Fig. 21 and Fig. 22, respectively. The harmonics component analysis of the full load is given in Fig. 23. The current THD analysis at different loads by adopting the modified PR regulator with active damping is compared to that obtained by adopting the traditional PI controller with normal DPC-SVM, as shown in Fig. 24. Fig. 25 shows the experimental waveforms of the DC

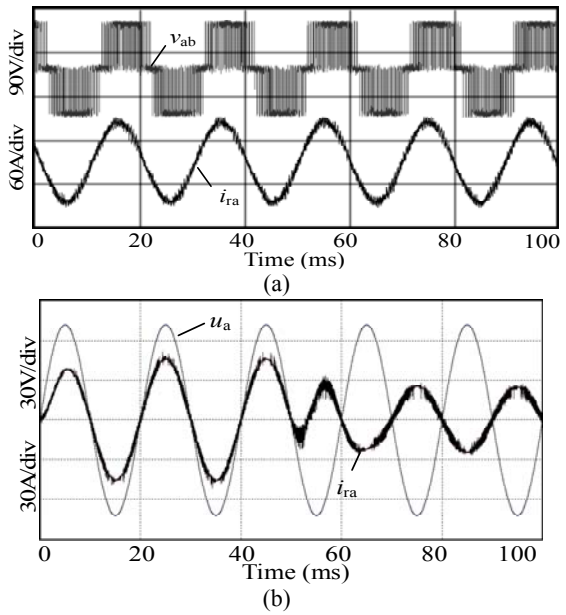

Fig. 17. Waveforms of converter side current and voltage. (a) Current and voltage of converter side. (b) Line voltage vs converter side current.

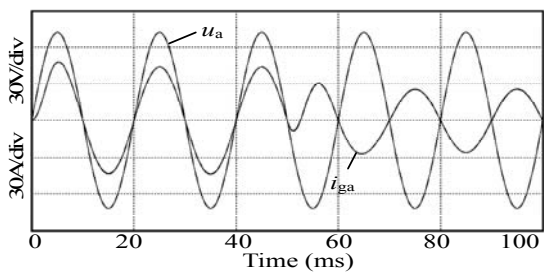

Fig. 18. Waveforms of grid side A-phase voltage and current.

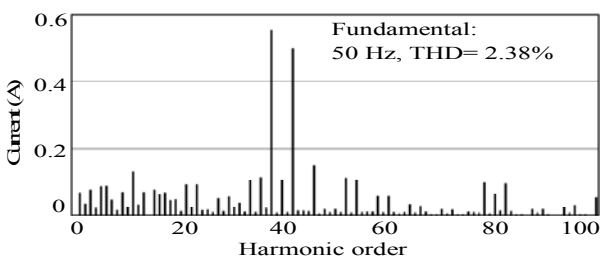

Fig. 19. Current spectrum of phase A.

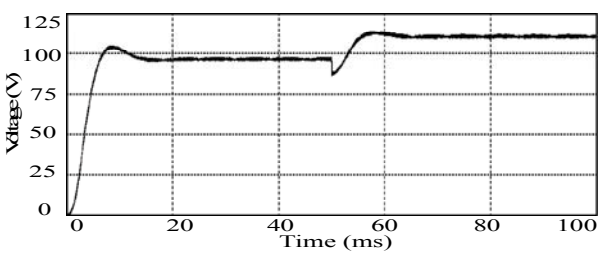

Fig. 20. DC-Link voltage dynamic response.

voltage and line current transient response with less over shoot of the DC bus reference voltage track. The reference for the active power has been varied in five steps with a constant zero reactive power. Each of them

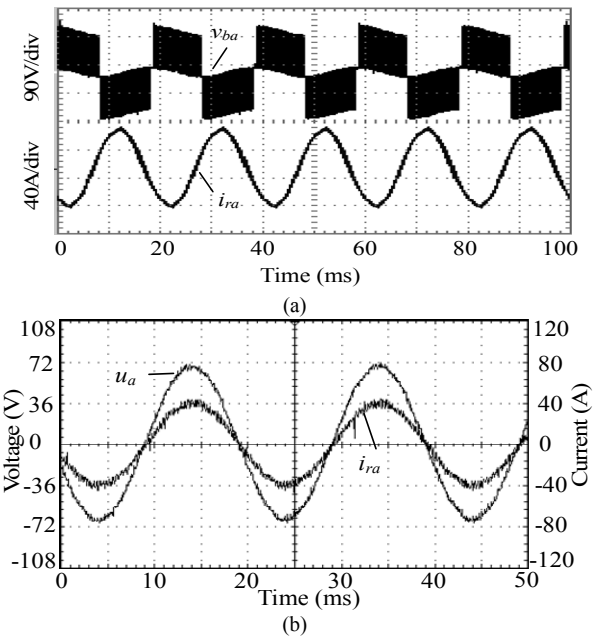

Fig. 21. Experimental waveforms of converter side current and voltage. (a) Current and voltage of converter side. (b) Line voltage vs converter side current.

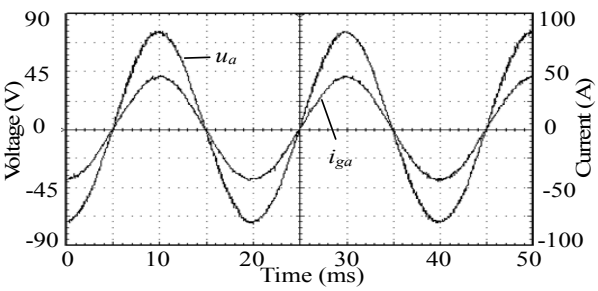

Fig. 22. Experimental waveforms of line side voltage and current.

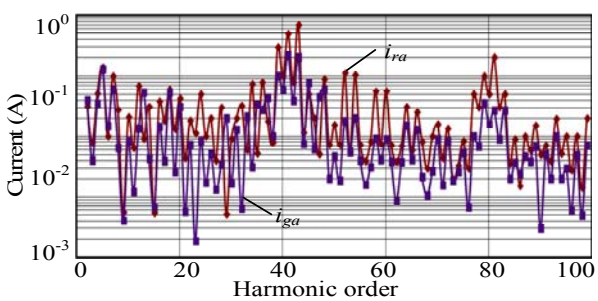

Fig. 23. Experimental input current spectrum of phase A.

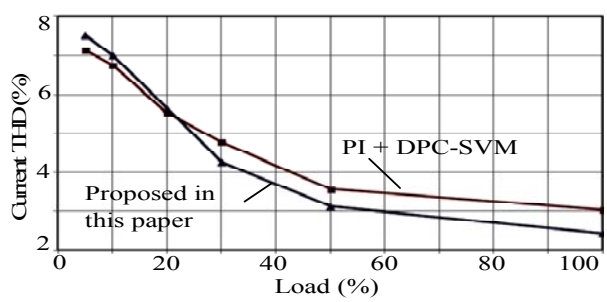

Fig. 24. THD comparison chart of grid side phase current.

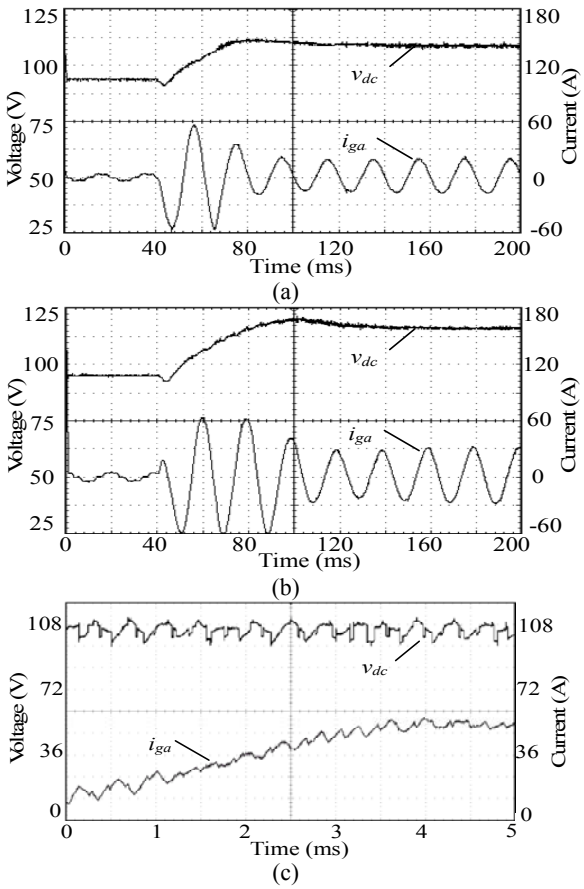

Fig. 25. Experimental waveforms of DC voltage transient response. (a) DC voltage step from 93V to 106V. (b) DC voltage step from 93V to 118V. (c) Zoom-in graphic of Fig. 25(a).

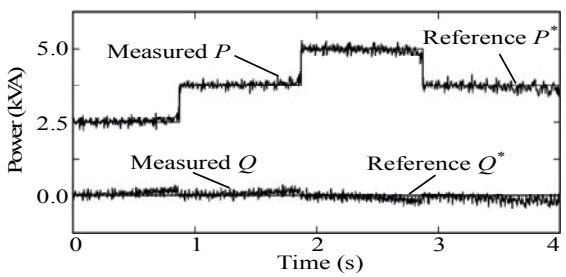

Fig. 26. Dynamic response of reference and measured power value.

has a width of 100ms. The given and measured power components are plotted in Fig. 26 with good dynamic track performance. It can be concluded that the proposed algorithm can improve the quality of the grid current, and that the robustness of the controller is verified through experimental results in accordance with the simulation results.

V. CONCLUSION

This paper presented a theoretical analysis of the inductance voltage vector control strategy based on a Proportional Resonant regulator under the stationary $\alpha\beta$ frame and the stability robustness approach for a three-phase VSC with respect to an optimum parameter match. To achieve an appropriate inductance voltage vector for each sector with accurate calculations on the current error to modulate the PWM converter, the judgment rule of sector selection and the optimal switch state by the geometrical distribution model is established. This can replace the trigonometric function calculation, Park transformation, real-time detection of the PLL and feed-forward decoupling used in the traditional space vector modulation. The proposed strategy with an active damping LCL filter achieves tracking errors of the dynamic instantaneous power via the application of the required inductance voltage vector under the stationary $\alpha\beta$ coordinate during each switching period. In addition, the PR controller is designed and discretized by means of the frequency response of the zero-pole assignment matching and cancellation with an in-depth performance influence analysis, which is frequently encountered when considering a system's robustness in the presence of parameter fluctuations and regulator digital discretization of a current-controlled VSC. The methodology to analyze and enhance the transient response of the inner current loop, based on the study of the system's transfer function locus through pole–zero placement, is also discussed. The optimal gain margin and phase margin are configured to get a rapid and non-oscillating transient response. Finally, the feasibility and effectiveness of the proposed design method are verified by the means of simulation and experimental results on a laboratory PWM converter prototype.

ACKNOWLEDGMENT

This work was supported by the National Natural Science Foundation of China (50977063), and the National High Technology Research and Development Program of China (863 Program) (2013BAG01B00, 2011AA11A279).

REFERENCES

[1] E. Koutroulis and F. Blaabjerg, "Design optimization of transformerless grid-connected PV inverters including reliability," *IEEE Trans. Power Electron.*, Vol. 28, No. 1, pp. 325–335, Jan. 2013.

[2] K. X. Wei, Q. Sun, B. Liang, and M. X. Du, "The research of adaptive fuzzy PID control algorithm based on LQR approach in DC-DC converter," in *the Proceedings of the IEEE Pacific-Asia Workshop on Computational Intelligence and Industrial Application*, Vol. 1, pp. 139-143, Dec. 2008.

[3] K. X. Wei and Q. Sun, "Automatic timing control algorithm for high power factor reversible converter," *Power System Technology*, Vol. 33, No. 16, pp. 49–52, Aug. 2009.

[4] F. Blaabjerg, R. Teodorescu, M. Liserre, and A. Timbus, "Overview of control and grid synchronization for distributed power generation systems," *IEEE Trans. Ind. Electron.*, Vol. 53, No. 5, pp. 1398–1409, Oct. 2006.

[5] K. X. Wei, Q. Sun, and J. Z. Feng, "Switching frequency control algorithm in three-phase rectifier using DSP," *High Voltage Engineering*, Vol. 35, No. 11, pp. 2853-2857, Nov. 2009.

[6] B. Bouaziz, F. Bacha, and M. Gasmi, "A sliding mode approach into constant switching frequency direct power control of a grid connected voltage source converter," *International Journal on Electrical Engineering & Informatics*, Vol. 7, No. 1, pp. 42-58, Mar. 2015.

[7] J. Shi and S. H. Li, "Analysis and compensation control of dead-time effect on space vector PWM," *Journal of Power Electronics*, Vol. 15, No. 2, pp. 431-442, Mar. 2015.

[8] M. H. N. Talib, Z. Ibrahim, N. A. Rahim, and A. S. A. Hasim, "Implementation of space vector two-arm modulation for independent motor control drive fed by a five-leg inverter," *Journal of Power Electronics*, Vol. 14, No. 1, pp. 115-124, Jan. 2014.

[9] J. Dannehl, C. Wessels, and F. W. Fuchs, "Limitations of voltage-oriented PI current control of grid-connected PWM rectifiers with LCL filters," *IEEE Trans. Ind. Electron.*, Vol. 56, No. 2, pp. 380–388, Feb. 2009.

[10] A. Bouafia, J.-P. Gaubert, and F. Krim, "Predictive direct power control of three-phase pulsewidth modulation (PWM) rectifier using space-vector modulation (SVM)," *IEEE Trans. Power Electron.*, Vol. 25, No. 1, pp. 228–236, Jan. 2010.

[11] J. Alonso-Martinez, J. E. Carrasco, and S. Arnaltes, "Table-based direct power control: a critical review for microgrid applications," *IEEE Trans. Power Electron.*, Vol. 25, No. 12, pp. 2949–2961, Dec. 2010.

[12] J. A. Restrepo, J. M. Aller, J. C. Viola, A. Bueno, and T. Habetler, "Optimum space vector computation technique for direct power control," *IEEE Trans. Power Electron.*, Vol. 24, No. 6, pp. 1637–1645, Jun. 2009.

[13] P. Mattavelli, "An improved deadbeat control for UPS using disturbance observers," *IEEE Trans. Ind. Electron.*, Vol. 52, No. 1, pp. 206–212, Feb. 2005.

[14] Y. A. R. I. Mohamed and E. F. El-Saadany, "Adaptive discrete-time grid-voltage sensorless interfacing scheme for grid-connected DG-inverters based on neural-network identification and deadbeat current regulation," *IEEE Trans. Power Electron.*, Vol. 23, No. 1, pp. 308–321, Jan. 2008.

[15] J. B. Hu, "Improved dead-beat predictive DPC strategy of grid-connected DC–AC converters with switching loss minimization and delay compensations," *IEEE Trans. Ind. Informat.*, Vol. 9, No. 2, pp. 728-738, May 2013.

[16] J. Dannehl, F. W. Fuchs, S. Hansen, and P. B. Thøgersen, "Investigation of active damping approaches for PI-based current control of grid-connected pulse width modulation converters with LCL filters," *IEEE Trans. Ind. Appl.*, Vol. 46, No. 4, pp. 1509-1517, Jul./Aug. 2010.

[17] C. L. Bao, X. B. Ruan, X. H. Wang, W. W. Li, D. H. Pan, and K. L. Weng, "Step-by-step controller design for LCL-type grid-connected inverter with capacitor–current-feedback active-damping," *IEEE Trans. Power Electron.*, Vol. 29, No. 3, pp. 1239-1253, Mar. 2014.

[18] D. G. Holmes, T. A. Lipo, B. P. Mcgrath, and W. Y. Kong, "Optimized design of stationary frame three phase AC current regulators," *IEEE Trans. Power Electron.*, Vol. 24, No. 11, pp. 2417-2426, Nov. 2009.

[19] L. Harnefors, A. G. Yepes, A. Vidal, and J. Doval-Gandoy, "Passivity-based controller design of grid-connected VSCs for prevention of electrical resonance instability," *IEEE Trans. Ind. Electron.*, Vol. 62, No. 2, pp. 702-710, Feb. 2015.

[20] A. Timbus, M. Liserre, R. Teodorescu, P. Rodriguez, and F. Blaabjerg, "Evaluation of current controllers for distributed power generation systems," *IEEE Trans. Power Electron.*, Vol. 24, No. 3, pp. 654-664, Mar. 2009.

[21] M. Abusara, S. M. Sharkh, and P. Zanchetta, "Control of grid-connected inverters using adaptive repetitive and proportional resonant schemes," *Journal of Power Electronics*, Vol. 15, No. 2, pp. 518-528, Mar. 2015.

[22] B. Li, M. Zhang, L. Huang, L. J. Hang, and L. M. Tolbert, "A robust multi-resonant PR regulator for three-phase grid-connected VSI using direct pole placement design strategy," in *the Twenty-Eighth Annual IEEE Applied Power Electronics Conference and Exposition(APEC)*, pp. 960-966, 2013.

[23] Z. Zeng, J. Yang, S. Chen, and J. Huang, "Fast-transient repetitive control strategy for a three-phase LCL filter-based shunt active power filter," *Journal of Power Electronics*, Vol. 14, No. 2, pp. 392-401, Mar. 2014.

[24] X. Wang, F. Blaabjerg, and C. Chen, "Autonomous control of inverter-interfaced distributed generation units for harmonic current filtering and resonance damping in an islanded microgrid," *IEEE Trans. Ind. Appl.*, Vol. 50, No. 1, pp. 452–461, Jan./Feb. 2014.

[25] J. Dannehl, M. Liserre, and F. W. Fuchs, "Filter-based active damping of voltage source converters with LCL filter," *IEEE Trans. Ind. Electron.*, Vol. 58, No. 8, pp. 3623–3633, Aug. 2011.

[26] S. G. Parker, B. P. McGrath, and D. G. Holmes, "Regions of active damping control for LCL filters," *IEEE Trans. Ind. Appl.*, Vol. 50, No. 1, pp. 424–432, Jan./Feb. 2014.

[27] R. Pena-Alzola, M. Liserre, F. Blaabjerg, R. Sebastián, J. Dannehl, and F. W. Fuchs, "Analysis of the passive damping losses in LCL-filter based grid converters," *IEEE Trans. Power Electron.*, Vol. 28, No. 6, pp. 2642-2646, Jun. 2013.

[28] J. Xu, S. Xie, and T. Tang, "Active damping-based control for grid-connected LCL-filtered inverter with injected grid current feedback only," *IEEE Trans. Ind. Electron.*, Vol. 61, No. 9, pp. 4746-4758, Sep. 2014.

[29] A. Vidal, A. G. Yepes, F. D. Freijedo, J. Malvar, Ó. López, and J. Doval-Gandoy, "A technique to estimate the equivalent loss resistance of grid-tied converters for current control analysis and design," *IEEE Trans. Power Electron.*, Vol. 30, No. 3, pp. 1747–1761, Mar. 2015.

[30] A. G. Yepes, A. Vidal, J. Malvar, Ó. López, and J. Doval-Gandoy, "Tuning method aimed at optimized settling time and overshoot for synchronous proportional-integral current control in electric machines," *IEEE Trans. Power Electron.*, Vol. 29, No. 6, pp. 3041–3054, Jun. 2014.

[31] L. Harnefors, A. G. Yepes, A. Vidal, and J. Doval-Gandoy, "Passivity-based stabilization of resonant current controllers with consideration of time delay," *IEEE Trans. Power Electron.*, Vol. 29, No. 12, pp. 6260–6263, Dec. 2014.

[32] C. Zou, B. Liu, S. Duan, and R. Li, "Influence of delay on system stability and delay optimization of grid-connected inverters with LCL filter," *IEEE Trans. Ind. Informat.*, Vol. 10, No. 3, pp. 1775-1784, Aug. 2014.

[33] A. G. Yepes, F. D. Freijedo, J. Doval-Gandoy, Ó. López, J. Malvar, and P. Fernandez-Comesaña, "Effects of discretization methods on the performance of resonant controllers," *IEEE Trans. Power Electron.*, Vol. 25, No. 7, pp. 1692–1712, Jul. 2010.

Qiang Sun was born in Shandong Province, China. He received his B.S. and M.S. degrees from the Tianjin University of Technology, Tianjin, China, in 2007 and 2010, respectively. He is presently working towards his Ph.D. degree in the School of Electrical Engineering and Automation, Tianjin University, Tianjin, China. In 2010, he was with Samsung Electro-Mechanics Co., Tianjin, China, where he worked on the research and development of electromechanical system applications. Since 2011, he has been with SIEMENS Electrical Drives Ltd., Tianjin, China, where he is working on the research and development of power electronics. His current research interests include power electronics technology, EMC mechanisms and control theory for power converters, electric vehicles and power quality.

Kexin Wei was born in Tianjin, China. He received his B.S. and M.S. degrees from Tianjin University, Tianjin, China, in 1978 and 1988, respectively. He was a Visiting Scholar at the Delft Technology University, Delft, Netherlands, and at Texas A&M University, College Station, Texas, in 1994 and 2000, respectively. Since 1997, he has been a Professor in the School of Electrical Engineering, Tianjin University of Technology, Tianjin, China, and a part-time Professor at Tianjin University. He is presently working as the Head of the Tianjin Key Laboratory of Control Theory and Applications in Complicated Systems and as the Vice-president of the Tianjin University of Technology. His current research interests include power electronics technology and control theory for power converters, electric vehicles and power quality.

Chenghai Gao was born in Henan Province, China. He received his B.S. degree from the Xi'an University of Architecture Science, Xi'an, China, in 1991; and his M.S. degree in the School of Electrical Engineering and Automation, Tianjin University, Tianjin, China, in 2010. He is presently working towards his Ph.D. degree in the School of Electrical Engineering and Automation, Tianjin University. Since 1995, he has been with SIEMENS Electrical Drives Ltd., Tianjin, China, where he is working on the research and development of power electronics as a R&D manager. His current research interests include power electronics technology and control theory for power converters and power quality.

Shasha Wang was born in Shandong Province, China. She received her B.S. degree from Dezhou University, Dezhou, China, in 2008; and her M.S. degree from the Tianjin University of Technology, Tianjin, China, in 2011. Since 2011, she has been with the R&D Department, Tianjin EV Energies Co., Ltd., Tianjin, China, where she is working on BMS development for electric vehicles. Her current research interests include BMS technology and battery SOC characteristics.

Bin Liang was born in Tianjin, China. She received her B.S. degree from the Tianjin University of Technology, Tianjin, China, in 2004; and her M.S. and Ph.D. degrees from Tianjin University, Tianjin, China, in 2006 and 2013, respectively. She is presently working as a Lecturer in the School of Electrical Engineering, Tianjin University of Technology. Her current research interests include power electronics technology and EMC mechanisms.